### CONFERENCE PRE-PRINT

# IMPURITY ACCUMULATION AND RADIATION DYNAMICS IN ADVANCED SCENARIOS IN W7-X

D. ZHANG, B. BUTTENSCHOEN, J. BALDZUHN, S.A. BOZHENKOV, K.J. BRUNNER, O.P. FORD, A. LANGENBERG, T. ROMBA, M. WAPPL, H.M. SMITH, C.D. BEIDLER, J.-P. BÄHNER, G. FUCHERT, M. HIRSCH, J. KNAUER, H.P. LAQUA, E. PASCH, K. RAHBARNIA, F. REIMOLD, T. STANGE, A. VON STECHOW, TH. WEGNER AND THE W7-X TEAM

Max-Planck-Institut für Plasmaphysik

Greifswald, Germany

Email: daihong.zhang@ipp.mpg.de

T. GONDA Auburn University, Auburn, AL, United States of America

C. JOHNSON, N. PABLANT, Princeton Plasma Physics Laboratory Princeton, NJ, US

#### Abstract

This work reports the recent experimental observations about impurity accumulation and radiation dynamics in advanced scenarios with improved energy confinement time in the stellarator Wendelstein 7-X. In gas-fueled, high-power plasmas generated by electron cyclotron resonance heating (ECRH), both impurity and energy confinement are limited by turbulence transport so that the neoclassical predicted impurity accumulation in ion-root regime is absent, and impurity radiation is normally edge-localized. In scenarios of high performance (HP; defined as energy confinement time approaching or exceeding ISS04 scaling, i.e.,  $\tau_E/\tau_{ISS04} \ge 1$ ), evident plasma radiation in the inner plasma region ( $\rho \le 0.5$ ) have been observed by bolometer tomography, for which evidence of metallic impurities (such as Fe, Cu and W from plasma facing components) in addition to low-Z impurities (mainly C from graphite divertor units) is confirmed by VUV spectroscopy. This pronounced core impurity radiation appears under plasma conditions with steepened density gradient that suppresses the turbulence in W7-X plasmas. These impurity behaviors are believed to be associated with the neoclassical impurity convection in ion-root regimes, which consequently becomes important. Enhanced electric field strength in ion-root has been experimentally and theoretically obtained. The investigated scenarios cover (a) low ECRH power plasmas with pure recycled neutral fuel, (b) ECRH plasmas with pellet injection, and (c) combined NBI and ECRH plasmas. The analysis shows that in these HP phases the radiation fraction in the core ( $\rho$ <0.5) remains low ( $f_{rad,core}$ <15%) and the emissivity peaks 10–20 cm away from the plasma center. This work shows the possible ways to optimize turbulence and neoclassical transport to achieve HP plasmas with tolerable impurity dynamics in W7-X.

## I. INTRODUCTION

Handling impurities released from plasma-facing components (PFCs) in magnetically confined fusion devices remains a key challenge for the generation of high-performance plasmas [1]. While radiation cooling by impurities in the edge region is beneficial for protecting the PFCs, it can be detrimental in the core due to radiation cooling and dilution of the central plasma. In the neoclassically optimized Wendelstein 7-X (W7-X) stellarator [2, 3], the most gas-fueled ECRH plasmas show no enrichment of impurities in the inner plasma region (hereinafter referred to as "impurity accumulation"), which is indicated by a short impurity transport time [3-6] ( $\sim$ 50–100 ms), much shorter than predicted by neoclassical theory, and by edge-localized, hollow impurity radiation profiles [7]. The latter resulted in favorable plasma detachment in a highly radiative regime [8-10], which is desirable for long-pulse plasma operation. However, these ECRH scenarios show a lower energy confinement time below the stellarator scaling law ( $\tau_{\rm E}/\tau_{\rm ISS04}$ <1) [11, 12] and an ion temperature limit at  $T_{\rm i,clamp} \sim$ 1.5 keV due to high levels of turbulent heat transport observed in the experiments [13].

Recently, high-performance (HP) plasmas with improved energy confinement  $(\tau_E/\tau_{ISS04} \ge 1)$  have been achieved in scenarios such as low-power ECRH with recycled hydrogen gas as fuel (i.e., gas supply turn-off)[14], pellet injections [15, 16], and a combination of ECRH and NBI [17]. All these scenarios show reduced particle and heat transport and an ion temperature exceeding the value of  $T_{i,clamp}$ , which is related to density-profile steeping that suppresses turbulence [18, 19] (typically of the ITG-type). However, bolometer tomography [20] has revealed an undesirable enhancement of core impurity radiation (at  $\rho < 0.5$ ) in these scenarios. VUV spectroscopy [21] has

confirmed that line emissions from metal impurities (such as Fe, Cu, and W), which add to the emission of low-Z impurities (C, O), play a key role. These impurities have different origins in the W7-X PFCs, such as carbon divertor target plates, stainless steel vacuum vessels, NBI beam ducts, and interlayers in wall protection structures (which contain Cu), and tungsten-coated tiles for investigating W erosion. These experimental observations indicate an impurity accumulation process in which neoclassical inward convection V<sub>neo</sub>, driven by the electric field of the ion-root ( $E_r$ <0), plays a central role in this process.

In source-free plasma regions, the impurity density  $n_z$  depends strongly on the normalized convection, defined as the ratio of the convection parameter to the diffusion coefficient,  $V^* = V/D$ ) [22], i.e.,  $n_Z \propto n_{Z,edge} e^{-\int_r^r e dge} \frac{V(\vec{r})}{D(\vec{r})} d\vec{r} \; ,$ 

$$n_Z \propto n_{Z,edge} e^{-\int_r^{r_edge} \frac{V(r)}{D(\tilde{r})} d\tilde{r}},$$
 (1)

where  $n_{Z,edge}$  is the impurity density at the plasma edge, determined by the impurity flux from the wall  $(\Gamma_w)$  and edge impurity transport. According to neoclassical theory in stellarators, the normalized neoclassical convection velocity of impurities,  $V_{neo}^*$  is related to the radial electric field  $E_r$  as

$$V_{neo}^* = \frac{q_z E_r}{T_z} - \left(\frac{D_z^2}{D_1^2} - \frac{3}{2}\right) \frac{1}{T_z} \frac{dT_z}{dr},\tag{2}$$

 $V_{neo}^* = \frac{q_z E_r}{T_z} - \left(\frac{D_z^Z}{D_1^Z} - \frac{3}{2}\right) \frac{1}{T_z} \frac{dT_z}{dr},$ where  $D_1^z$  and  $D_2^z$  are transport coefficients [23] that depend on collisionality, the electric field, magnetic topology, and impurity charge state Z. Outward convection  $(V_{neo}>0)$  is usually associated with the electron-root  $(E_r>0)$  at low collisionality (e.g., when  $T_e \gg T_i$ ), while inward convection ( $V_{neo} < 0$ ) is typically associated with the ion-root  $(E_r < 0)$  at high collisionality.

Since the impurity radiation is strongly correlated with the impurity density  $n_z$ , the radiation profile is shaped by the values of  $V^*$ :

$$\varepsilon_{rad}(\mathbf{r}) \propto \mathbf{n}_e(r) \mathbf{n}_{Z,edge} L_Z(Z_0, T_e) e^{-\int_r^{T_edge} V^* d\tilde{r}}$$
 (3)

where  $L_Z$  is the radiative power-loss function of the impurity with atomic number  $Z_0$  [24]. This function is sensitive to the electron temperature  $T_e$  and is further influenced by impurity transport. In regimes where turbulent transport is suppressed, neoclassical impurity transport typically dominates, i.e.,  $V^* \approx V_{neo}^*$ . Under such conditions, the impurity density profile  $n_z(\mathbf{r})$  —characteristic of the ion-root regime—exhibits a peaking factor that scales with Z. Consequently, the resulting radiation profile  $\varepsilon_{\rm rad}(r)$  becomes more strongly peaked than the electron density profile in the plasma core.

This work provides impurity radiation behaviours in selected W7-X scenarios with improved energy confinement times,  $\tau_E$ , extending from several up to several tens of  $\tau_E$ . It represents a first step toward identifying the operational windows of W7-X in which impurities can remain in the plasma core without significantly degrading overall performance.

#### II. EXPERIMENTAL OBSERVATIONS

The improvement in energy confinement t in W7-X plasmas has been recently analysed using a broader database on turbulent heat transport in a variety of scenarios [19]. This reaffirms earlier studies in which the normalized gradients of density  $a/L_n$  ( $L_n = -(d\ln n_e/dr)^{-1}$ ) and ion temperature  $a/L_T$  ( $L_T = -(d\ln T_i/dr)^{-1}$ ) were identified as the primary parameters governing turbulent transport [25-27] (e.g., ITG-type in most ECRH scenarios). The present database reveals a systematic suppression of this ITG turbulent transport with increasing  $a/L_n$  in W7-X plasmas

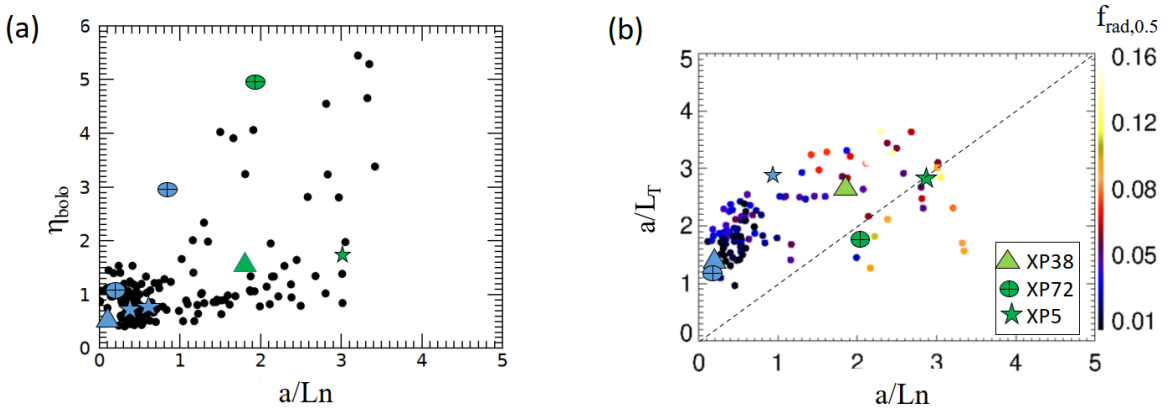


FIG. 1 Core radiation levels, (a) ratio of chord-brightness between core and edge bolometer channels,  $\eta_{bolo}$ , and (b) radiation fraction  $f_{rad,0.5}$  as a function of a/Ln and  $a/L_T$  at mid-radius.

(see Fig. 14 in Ref.[19]). This suppression is most pronounced in the ion channel and less evident in the electron channel. All plasmas with  $\tau_E/\tau_{ISS04} > 1$  feature increased density gradients that are largely independent of the magnetic configuration. A critical threshold is identified at  $a/L_n > 1$  (for  $\rho \approx 0.5$ ), above which turbulence suppression alters heat transport, consistent with the observed changes in impurity transport [28]. This transition leads to a central C6+ density peaking, as confirmed by measurements with charge-exchange recombination spectroscopy (CXRS) (see also Fig.7(c)).

The plasma phases included in the database of Ref.[19] are also used to identify impurity core radiation. The ratio of the chord brightness (i.e., the line-averaged emissivity) detected by the core bolometer channel to that detected by the edge channel,  $\eta_{\text{bolo}}$ , is shown in Fig. 1(a) as a function of the density gradient  $a/L_n$ . For  $a/L_n < 1$ ,  $\eta_{\text{bolo}}$  scatters around unity, whereas for  $a/L_n > 1$  it tends to increase up to  $\eta_{\text{bolo}} \sim 5$ . This high level of  $\eta_{\text{bolo}}$  indicates enhanced core radiation (which is normally used as an indicator of impurity accumulation). The radiated power inside r/a < 0.5,  $P_{\text{rad},0.5}$ , is determined by bolometer tomography, and its corresponding fraction,  $f_{\text{rad},0.5} = P_{\text{rad},0.5}/P_{\text{heat}}$ , is further calculated using the total heating power  $P_{\text{heat}}$ . Its dependence on  $a/L_n$  and  $a/L_T$  is shown in Fig. 1(b). It can be seen that as  $a/L_n$  increases, the values of  $f_{\text{rad},0.95}$  increase from a few percent for  $a/L_n < 1$  to up to  $\sim 15\%$  for  $a/L_n > 1$ . The larger symbols filled in green are the selected HP scenarios with the normalized energy confinement

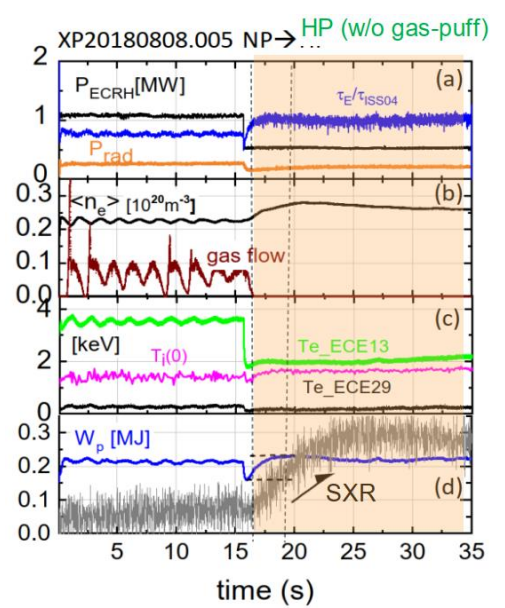


FIG.2. Time traces of diagnostics in XP20180808.005.

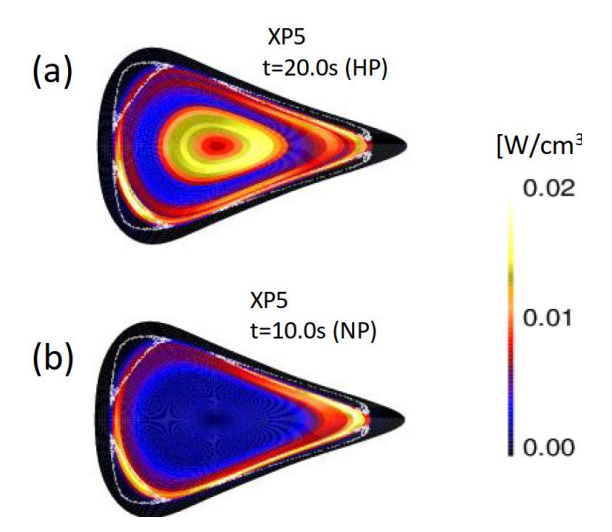


FIG.3 The 2D radiation patterns obtained by bolometer tomography for selected time points in the HP and NP phases for XP5.

time, defined as  $\eta_{\tau=}\tau_E/\tau_{ISS04}\geq 1$ , while the same symbols in blue denote the normal plasma (NP) phases in the discharges studied.

# 2.1 Low-power ECRH plasma

We briefly describe the experimental findings in program XP20180808.005 (hereafter referred to as XP5). Details can be found in [14]. Fig. 2 shows the time evolution of the key diagnostics. The hydrogen plasma is generated by ECRH with an initial power of PECRH =1.2MW, which is later reduced to 0.5 MW. During the first phase, gas puffing is actively regulated but is subsequently switched off automatically by feedback control at t=16s, shortly after the reduction of PECRH (see the first vertical dashed line in Fig.1). Following this change, the plasma gradually transitions to a HP phase, characterized by 1) recovery of the plasma stored energy  $W_p$  despite the halved  $P_{ECRH}$ ; 2) a slight increase of ion temperature above the clamp level  $T_{i,clamp}$ , and 3) a rise in plasma density  $\langle n_e \rangle$  despite the turn-off of gas-supply. In the HP phase, the plasma achieves an energy confinement time  $\tau_E = 0.4$  s and a normalized energy confinement time  $\eta_{\tau}$  ~1, both significantly higher than those in the preceding normal performance (NP) phase (t < 16.0 s), where  $\tau_E = 0.2 \text{ s}$ and  $\eta_{\tau} = 0.7$ .

The soft x-ray (SXR) signal detected by the bolometer system increases substantially during the build-up of the HP phase, and further increases after  $W_p$  stabilized. Its rise time of ~5 s indicates a long impurity transport time, far exceeding the typical values in conventional plasmas (~50-100 ms) but comparable to neoclassical predictions. Tomographic reconstructions of the 2D radiation profiles (Fig. 3) reveal enhanced radiation intensity in the inner plasma region ( $\rho < 0.5$ ) consistent with the SXR increase. The fraction of the total radiation loss inside  $\rho < 0.5$  is  $f_{rad,0.5} \sim 10\%$ . This SXR emission is primarily attributed to Fe-impurity ions (Z=21), as identified by VUV spectroscopy and a pulse height analysis system (see Fig.7 in Ref.[14]).

In the HP phases, the maximum emissivity reaches  $\varepsilon_{rad,m} \sim 15.0 \text{ mW/cm}^3$ , located at  $\rho \sim 0.3$ . 1D impurity transport analysis shows that 1) for  $\rho < 0.5$ , the diffusion coefficient is low  $(D \sim 0.02 \text{ m}^2/\text{s})$ ,  $\sim 10 \text{ times lower than typical turbulent transport and consistent with neoclassical predictions; 2) A reversal of impurity convection <math>(V)$  occurs near the radiation peak, where impurity accumulation is observed, coinciding with the  $E_r$  transition from electron-root to ion-root as measured by x-ray imaging crystal spectrometer (XICS) diagnostics [29] (Fig. 12 in Ref[14].). The transition from NP to HP phase occurs when the gas supply is turned off, leaving only recycling neutrals as the fuelling source. This results in the edge plasma density decrease and a subsequent steepening of the  $n_e$ -profile (Fig.4 in [9])). The density and temperature gradient lengths become similar  $(\eta_i = (a/L_T)/(a/L_n) \approx 1)$  (see Fig.1(b)), aligning with "stability valley" conditions (Fig.14 in [9]), where micro-instabilities like ITG turbulence are suppressed [10]. These results suggest that edge fuelling details under certain plasma conditions can play a critical role in shaping the density profile and thereby regulating turbulent transport.

### 2.2 Pellet refueled ECRH discharges

In the 2018 experimental campaign, the injection of hydrogen pellets into W7-X ECR-heated plasmas demonstrated its core fuelling capability, resulting in a steeper density profile [15, 16]. The turbulence in the plasma is stabilized after pellet injections, which was diagnosed experimentally by the phase contrast imaging (PCI) system [3, 27]. HP plasma phases with improved energy confinement and increased central electron and ion temperatures,  $T_e(0)$  and  $T_i(0)$ , were achieved. Temporarily, the value of  $\tau_E$  exceeds the value of  $\tau_{ISS04}$  by more than 30%. In the most recent campaign (2024-2025), a new pellet fuel system has been applied and can inject a continuous, rapid stream of solid hydrogen pellets, thereby supplying the core plasma with fuel more effectively. Fig. 4 (a-j) shows time series of key plasma parameters and line emissions of impurity ions as well as bolometer measurements in a selected discharge example XP20241121.038 (hereafter XP38). The reason for the selection in this study is the low variation in plasma parameters during HP formation and a longer duration of this phase

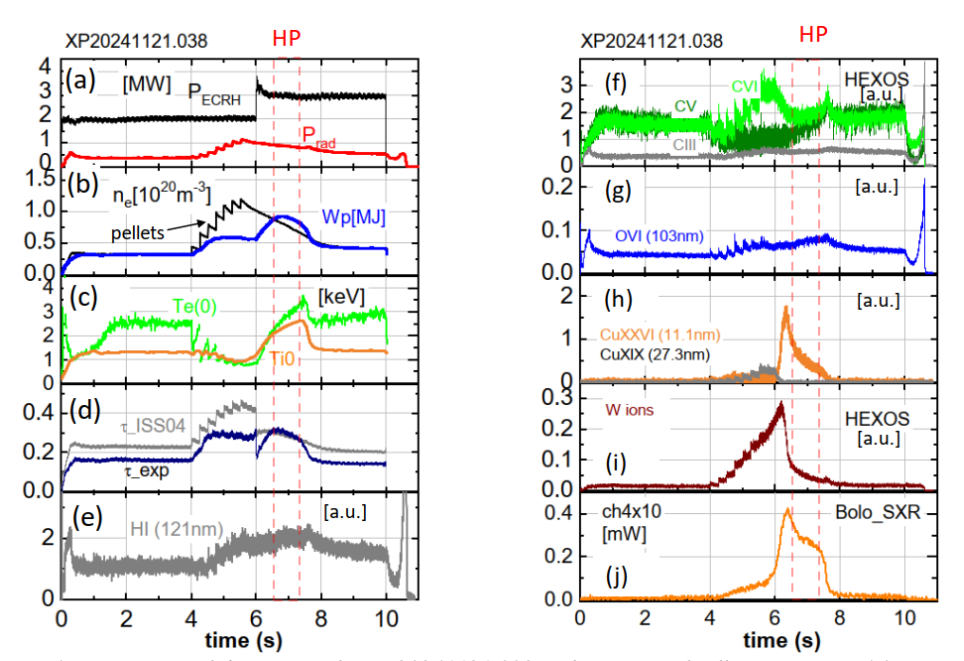


FIG. 4. Time traces of diagnostics for XP20241121.038 with a series of pellet injections (4.0s-5.5s).

(marked by dashed rectangles), which facilitates the investigation of impurity transport. During pellet injections, central densities  $T_e(0)$  of up to  $1.6\times10^{20}\,$  m<sup>-3</sup> are achieved using 2MW ECR-heating (see Fig. 4 (b)). However, the enclosed plasma energy is low due to the low temperature values (~1.0 keV for both  $T_e(0)$  from the TS systemand the line-averaged ion temperature  $T_{i0}$  from the central channel of the XICS system). The HP phase then gradually forms after ~0.5 s of injections with increased  $P_{ECRH}$  (up to 3 MW); both  $T_e(0)$  and  $T_{i0}$  simultaneously rise to ~2.5 keV. The plasma stored energy reaches  $W_p$  of ~0.9 MJ and an energy confinement time  $\tau_E \sim 0.3$  s. This value of  $\tau_E$  reaches the ISS04 scaling, as shown in Fig. 3(d) (labelled  $\tau_E$  and  $\tau_E$  and  $\tau_E$  from the corresponding a/ $L_T$  and a/ $L_T$  values at  $\rho = 0.5$  are shown in Fig. 1(b), equivalently  $\eta_i = (a/L_T)/(a/L_n) \approx 1.4$ . The HP phase lasts for about ~1s (more than three times  $\tau_E$ ) and then transitions to an NP phase at t~7.4s when  $T_e(0)$ 

The most important observations regarding the radiation from impurities are as follows:

significantly exceeds the central line-averaged ion temperature (from XICS) T<sub>i0</sub> by ~1.0 keV.

- i. During pellet injections, almost all line emissions from impurity ions such as CVI, OVI, Cu18+, and W ions (quasi-continuum; from multi-W ions with Z~30-40) increase in response to the increase in density. The core channel and SXR channel in the bolometer system detect a continuous increase in signal.
- ii. During the formation of the HP phase (t>6s), the line emissions of Cu25+ (labeled CuXXVI in Fig. 4(h)) and the quasi-continuum W-lines ( $\sim$ 5.18 nm) increase up to 6.2 s, which correlates with the SXR waveform. The strong increase in the SXR level is partly related to the increase in electron temperature ( $T_e(0)=1$  keV to  $\sim$ 2 keV), which triggers ionization processes of metal ions (e.g., Cu25+ has an ionization energy of  $E_{ion}=2.2$  keV and W30+ to W40+ have  $E_{ion}$  values of 1.4 keV to 2.1 keV). In contrast, the line emission of Cu18+, which is located in the outer plasma region (designated CuXIX;  $E_{ion}=0.64$  keV), decreases.
- iii. In the HP phase, all line emissions except CIII and OVI, which follow the waveform of HI (Lyman-α, 121.5nm; Fig. 3(e)), are reduced to a certain extent (Fig. 4 (f-g)). This reduction is related to the plasma parameter variation (see the density and temperature profiles measured with Thomson scattering (TS) (Fig. 5(a) and (b)). Further analysis and simulation of this impurity behavior is a task for future.
- iv. During the transition from HP to NP, indicated by a sharp drop in  $T_e(0)$  and  $T_{i0}$ , a small peak appears in impurity radiation (CV, CVI, OVI, and  $P_{rad}$ ). This feature is likely related to a fast MHD phenomenon occurring on a timescale much shorter than the typical confinement time [16]. After the transition, all line emissions from metal ions in the SXR range almost completely vanish, although  $T_e(0)$  remains sufficiently high to sustain their ionization. At t>8s, the central ion temperature  $T_i(0)$  drops to below  $T_{i,clamp}$  (see blue curves in Fig. 5(b)). These observations suggest that both variations in impurity influx  $\Gamma_w$  (see equation (1)) and impurity transport are necessary to account for the measured metallic ion radiation in the HP phase.

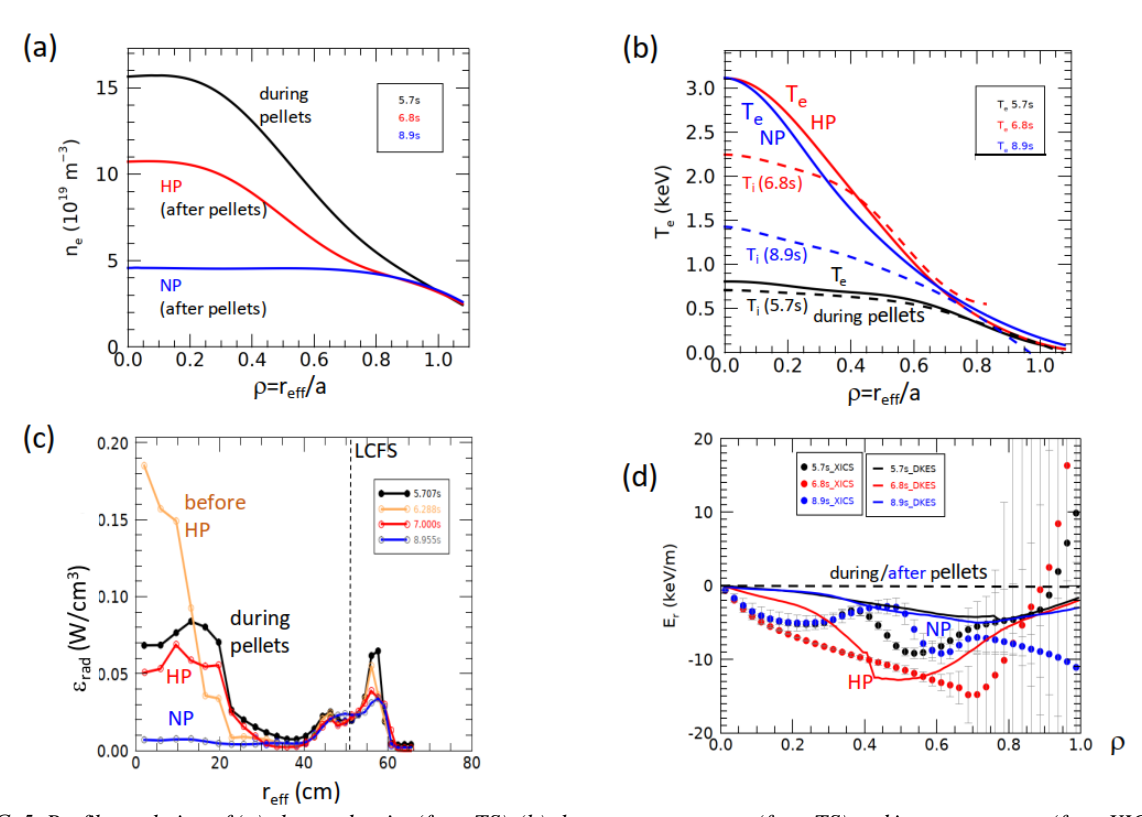


FIG. 5. Profile evolution of (a) plasma density (from TS), (b) electron temperature (from TS) and ion temperature (from XICS), (c) 1D radiated power density (from bolometer tomography), and (d) E<sub>r</sub>-profiles from XICS measurements and neoclassical theory for selected plasma phases in XP38 during and after pellet injections, including the HP and NP phases.

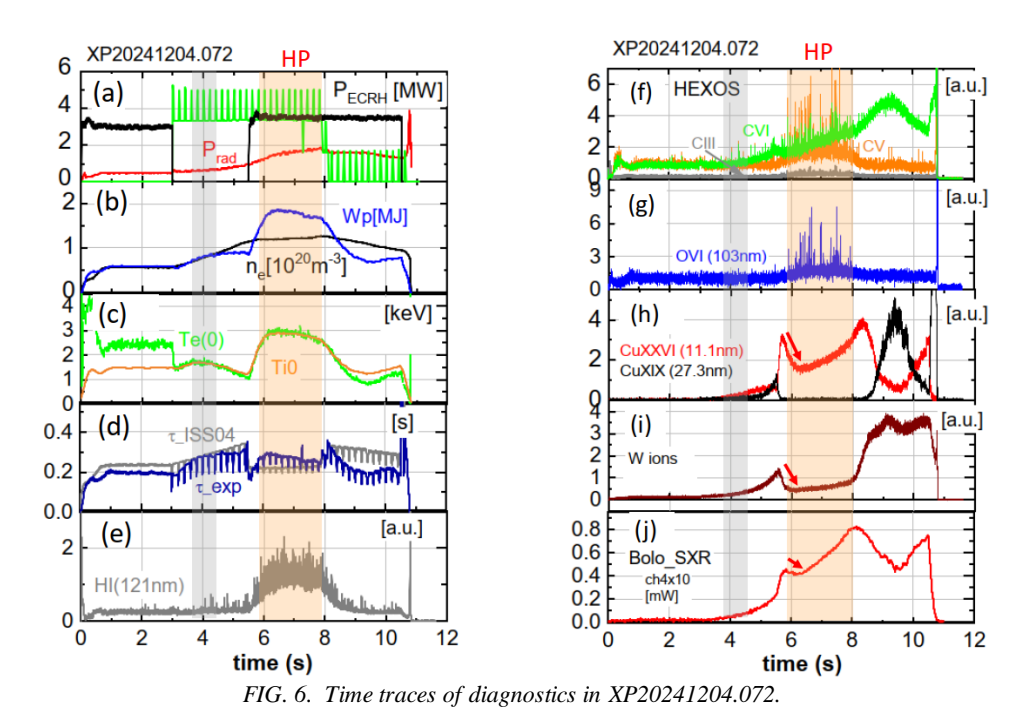
The radial radiation profiles derived from bolometer tomography for selected times are shown in Fig. 5(c). The strongest metallic-ion emissivity appears during the formation of the HP, exhibiting a centrally peaked profile. In the established HP phase, the maximum emissivity decreases in the plasma core and shifts off-axis, with the peak located ~10 cm from the plasma centre. In the NP phase, hollow radiation profiles are observed. The enhanced emission of metallic impurities in the inner plasma region during the HP phase indicates impurity enrichment, further supported by the fact that the 1D radiation profile is more strongly peaked in the core than the density profile (see Fig. 5 (c)). In this phase, radial  $E_r$  profiles obtained from the XICS measurements reveal an ion-root structure with enhanced amplitude in the plasma region  $\rho$ <0.7, with no electron-root region present in the core

features that are qualitatively consistent with neoclassical theory. A clearly defined ion-root region with  $E_r \sim 13$  kV/m at  $\rho \sim 0.5$  is shown in Fig. 5(d). Further analysis of impurity transport and radiation behaviour is envisaged.

# 2.3 Combined NBI and ECRH discharges

In NBI-heated W7-X plasmas, both density and temperature profiles differ from those in ECRH plasmas (with or without pellet injections), owing to the broader particle source and the more effective ion heating provided by NBI. These changes affects particle transport and often lead to impurity accumulation, as evidenced by central C6+ density peaking[28]. Pronounced line emissions from metal impurities (Cu and W ions) are frequently observed. The corresponding radiation profiles typically exhibit a central peak with a clearly higher peaking factor than the C6+ density profile, which can be attributed to contributions from metallic impurity ions (in accordance with Z-dependent neoclassical transport).

Sustained long-pulse discharges seems to be difficult to achieve because impurity radiation near the plasma axis increases continuously, cooling the plasma core and degrading performance. The application of additional ECRH power can mitigate impurity accumulation, but its exact effects on the density profile remain uncertain [17]. A



balanced increase in NBI and ECRH power to optimize the density profile is currently being investigated.

A well-optimized discharge, XP20241204.072 (hereinafter XP72), is selected for detailed analysis. Fig. 6(a-j) shows the time evolution of key diagnostic signals, including plasma parameters and impurity emissions. The discharge is initialized by a 3 MW ECRH scenario, followed by a 3 MW NBI phase during which the ECRH is switched off. After 3s of NBI heating, a 3.5 MW ECRH is reintroduced. The combined NBI+ECRH scenario lasts for 2.5 s, during which an HP phase develops after ~0.5 s. In this phase, the plasma energy reaches  $W_p \sim 1.8$  MJ, the energy confinement time improves to  $\tau_E \sim 0.3$  s (~1.5 times higher than the ISS04 scaling), and the central ion temperature rises to  $T_i(0)\sim 2.7$ keV (see also Fig. 6(b)), exceeding the value of  $T_{i,clamp}$ . These parameters correspond

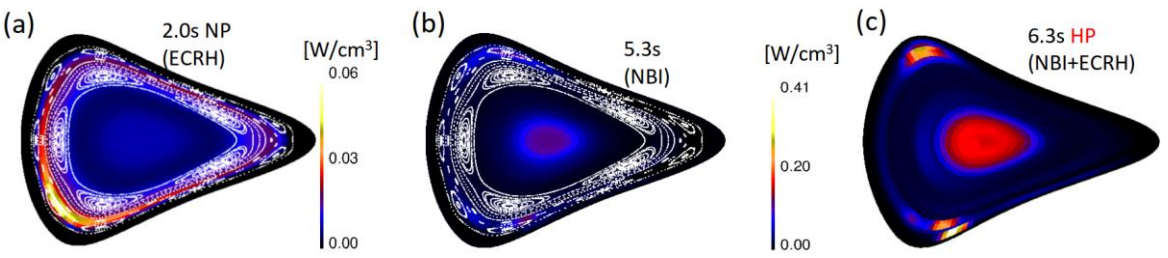


Fig.7. 2D radiation profiles obtained from bolometer tomography for different heating scenarios in XP72 (a) ECRH, (b) NBI, and (c) combined NBI and ECRH. The edge magnetic topology is overlaid as white Poincare plots in (a) and (b).

Panels (b) and (c) share the same color bar.

to the highest stellarator triple product  $(nT\tau_E > 10^{20} \text{ keV·m}^{-3} \cdot \text{s})$  reported to date. The stronger peaking of the electron density at the mid-plasma radius in the HP phase can be seen in Fig. 8(a); the corresponding a/L<sub>T</sub> and a/Ln values at  $\rho$ =0.5 are shown in Fig.1(b), equivalently  $\eta_i = (a/L_T)/(a/L_n) \approx 0.9$ . The reason for the slight decrease in W<sub>p</sub> during the HP phase is currently still being investigated.

The behavior of the impurities in different phases, compared to the ECRH phase, is as follows:

- **NBI scenario**: The line emissions from the metallic ions (Cu18+, Cu25+, and W ions) gradually increase with time, accompanied by a sustained increase in the SXR signal. This trend is partly attributed to the nearly linear rise of electron density over time, despite the absence of additional gas fueling. The increase continues even when the values of T<sub>e</sub>, T<sub>i</sub>, and W<sub>p</sub> decrease. Bolometer tomography shows significant core radiation (ρ<0.5) in contrast to the hollow radiation profiles observed in the ECRH scenario (see Figs. 7(a) and (b)). All this suggests that the impurity accumulation plays an important role. A peaked C6+ density profile in this phase is obtained by the CXRS measurement (see black symbols in Fig. 8(c)).
- **Combined NBI+ECRH:** After the reintroduction of ECRH, the total line emission from metallic ions initially decreases, as does the SXR signal. Subsequently, however, both rise continuously, suggesting that the impurity accumulation continues. This hypothesis is confirmed by the CXRS measurements, which show a peaked C6+ density profile with elevated levels during the later stage of the HP phase (see Fig. 8(c)). Note that fluctuations of low-Z impurity ion emissions (C III, C V, C VI, and O VI) observed during the HP phase are likely caused by MHD instabilities at the plasma edge.

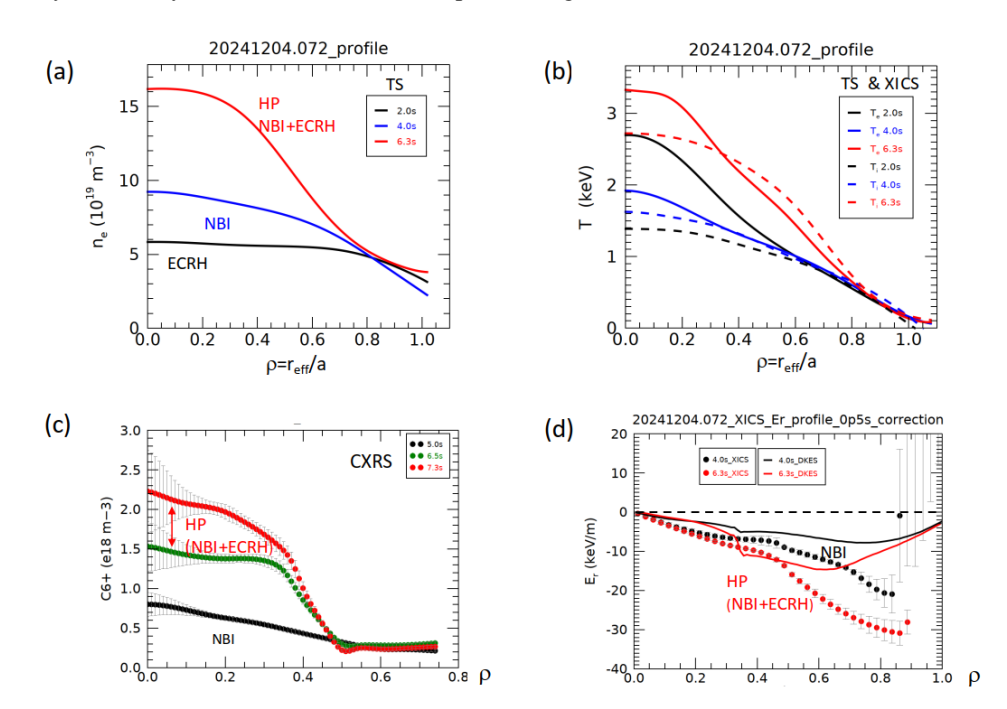


FIG. 8. Time evolution of plasma parameter profiles in discharge XP72: (a) density profiles from the TS system, (b) T<sub>e</sub> and T<sub>i</sub> profiles from TS and CXRS measurements, (c) C6+ density profiles from CXRS, and (d) E<sub>r</sub> profiles from XICS measurements (solid circles) and neoclassical predictions (solid lines).

After switching off the NBI power (t>8 s), the value of  $T_e(0)$  drops rapidly but did not return to the initial ECRH phase level, instead stabilizing at a low level corresponding to the ion temperature (~1 keV). Metal ion emission remained high, though the response varied by ion species with respect to the change in  $T_e$ . Weakly charged ions (CIII, CV, and OVI) follow the time evolution of the HI emission, similar to the behavior observed in pellet-fueled plasmas. In contrast, the CVI line emission continues to increase, reaching a maximum more than 1s after the end of the NBI, with the SXR signal reaching its minimum at this point. This discrepancy suggests that carbon ions contribute less to the SXR values compared to metallic impurities.

The central peaking of the radiation power profile, along with the increased emission of metallic ions in the inner plasma region, indicates impurity accumulation during the HP phase. Radial  $E_r$  profiles obtained from the XICS measurements reveal an "ion root" structure with enhanced amplitude for plasma regions  $\rho$ <0.8, similar to the HP

phase following pellet injections. A well-defined ion-root region with  $E_r \sim -15$  kV/m at  $\rho \sim 0.5$  is identified, in qualitative agreement with neoclassical theory predictions. These results are summarized in Fig. 8(d).

#### 3. SUMMARY

The dynamics of impurity radiation in representative HP scenarios at W7-X have been investigated, including low-power ECRH plasmas, pellet injection-fueled plasmas, and combined ECRH+NBI heating. Bolometer and spectroscopy diagnostics show that the central peaking of the radiation profiles is predominantly due to line emission from highly ionized metallic ions, such as Cu, Fe, and W. Low-Z impurities, such as C6+, are present but do not dominate the core radiation. This impurity behavior is believed to be due to neoclassical inward convection, which becomes significant when turbulence is suppressed and the corresponding diffusion does not counteract the inward convection, unlike in typical ECRH plasmas. The enhanced ion-root amplitudes identified by XICS diagnostics are qualitatively consistent with neoclassical predictions. The turbulence suppression is further evidenced by a stronger peaking of the electron density. The HP phases investigated exhibit a core radiation fraction f<sub>rad,core</sub>~10–15%, with the emissivity peaking 10–20 cm away from the plasma center or a more broadly distributed radiation zone. Ongoing analyses aim to determine the threshold f<sub>rad,core</sub> at which impurity radiation becomes the dominant energy loss channel, leading to confinement degradation. In addition, simulations of impurity radiation under actual plasma conditions in XP38 and XP72 are planned to confirm the role of neoclassical convection, as has already been done for low-power HP plasmas.

#### ACKNOWLEDGEMENTS

This work has been carried out within the framework of the EUROfusion Consortium, funded by the European Union via the Euratom Research and Training Programme (Grant Agreement No 101052200 — EUROfusion). Views and opinions expressed are however those of the author(s) only and do not necessarily reflect those of the European Union or the European Commission. Neither the European Union nor the European Commission can be held responsible for them.

# REFERENCES

- 1. Burhenn, R., et al., Nuclear Fusion, 2009. **49**(6): p. 065005.
- 2. Beidler, C.D., et al., Nature, 2021. **596**(7871): p. 221-226.
- 3. Klinger, T., et al., Nuclear Fusion, 2019. **59**(11): p. 112004.
- 4. Geiger, B., et al., Nuclear Fusion, 2019. **59**(4): p. 046009.
- 5. Langenberg, A., et al., Physics of Plasmas, 2020. **27**(5): p. 052510.
- 6. Wegner, T., et al., Journal of Plasma Physics, 2023. **89**(3): p. 955890302.
- 7. Zhang, D., et al., Nuclear Fusion, 2021. **61**(12): p. 126002.
- 8. Zhang, D., et al., Physical review letters, 2019. **123**(2): p. 025002.
- 9. Jakubowski, M., et al., Nuclear Fusion, 2021.
- 10. Feng, Y., et al., Nuclear Fusion, 2021. **61**(8): p. 086012.
- 11. Yamada, H., et al., Nuclear Fusion, 2005. **45**(12): p. 1684.
- 12. Fuchert, G., et al., Nuclear Fusion, 2020. **60**(3): p. 036020.
- 13. Beurskens, M.N., et al., Nuclear Fusion, 2021.
- 14. Zhang, D., et al., Plasma Physics and Controlled Fusion, 2023. 65(10): p. 105006.
- 15. Baldzuhn, J., et al., Plasma Physics and Controlled Fusion, 2020. **62**(5): p. 055012.
- 16. Bozhenkov, S., et al., Nuclear Fusion, 2020. **60**(6): p. 066011.
- 17. Ford, O., et al., Nuclear Fusion, 2024. **64**(8): p. 086067.
- 18. Bannmann, S., et al., Nuclear Fusion, 2024. **64**(10): p. 106015.
- 19. Wappl, M., et al., Plasma Physics and Controlled Fusion, 2024.
- 20. Zhang, D., et al., Nuclear Fusion, 2021. **61**(11): p. 116043.
- 21. Biel, W., et al., Review of scientific instruments, 2006. 77(10).
- 22. Fussmann, G., Nuclear fusion, 1986. 26(8): p. 983.
- 23. Van Rij, W. and S. Hirshman, Physics of Fluids B: Plasma Physics, 1989. 1(3): p. 563-569.
- 24. Summers, H. and R. McWhirter, Journal of Physics B: Atomic and Molecular Physics, 1979. 12(14): p. 2387.
- 25. Alcusón, J., et al., Plasma Physics and Controlled Fusion, 2020. **62**(3): p. 035005.
- 26. Carralero, D., et al., Nuclear Fusion, 2021. **61**(9): p. 096015.
- 27. Bähner, J.-P., et al., Journal of Plasma Physics, 2021. **87**(3): p. 905870314.
- 28. Romba, T., et al., Nuclear Fusion, 2023. **63**(7): p. 076023.
- 29. Pablant, N., et al., Nuclear Fusion, 2020. **60**(3): p. 036021.